

Virtual and Physical Prototyping

ISSN: 1745-2759 (Print) 1745-2767 (Online) Journal homepage: www.tandfonline.com/journals/nvpp20

Digital light processing 3D printing of large-scale and crack-free ceramics with perforated internal honeycomb structures

Siqian Wu, Rong Wang, Liuchao Jin , Xingjian Huang , Wuzhao Li , Kun Zhou & Qi Ge

To cite this article: Siqian Wu, Rong Wang, Liuchao Jin , Xingjian Huang , Wuzhao Li , Kun Zhou & Qi Ge (2025) Digital light processing 3D printing of large-scale and crack-free ceramics with perforated internal honeycomb structures, *Virtual and Physical Prototyping*, 20:1, e2589472, DOI: [10.1080/17452759.2025.2589472](https://doi.org/10.1080/17452759.2025.2589472)

To link to this article: <https://doi.org/10.1080/17452759.2025.2589472>



© 2025 The Author(s). Published by Informa UK Limited, trading as Taylor & Francis Group



Published online: 27 Nov 2025.



Submit your article to this journal



Article views: 15



View related articles



CrossMark

View Crossmark data

Digital light processing 3D printing of large-scale and crack-free ceramics with perforated internal honeycomb structures

Siqian Wu  ^a, Rong Wang  ^a, Liuchao Jin ^{a,b}, Xingjian Huang ^a, Wuzhao Li ^a, Kun Zhou  ^c and Qi Ge ^a

^aShenzhen Key Laboratory for Additive Manufacturing of High-Performance Materials, Department of Mechanical and Energy Engineering, Southern University of Science and Technology, Shenzhen, People's Republic of China; ^bDepartment of Mechanical and Automation Engineering, The Chinese University of Hong Kong, Hong Kong, People's Republic of China; ^cSingapore Centre for 3D Printing, School of Mechanical and Aerospace Engineering, Nanyang Technological University, Singapore, Singapore

ABSTRACT

Digital light processing (DLP) enables high-resolution and efficient ceramic additive manufacturing, yet the fabrication of large-scale, crack-free ceramic parts remains severely constrained by critical defects arising during debinding and sintering. To address this challenge, we propose an approach leveraging honeycomb sandwich structures with perforated sidewalls to mitigate crack formation. Key structural parameters, including the outer wall thickness (a) and honeycomb cell characteristics such as sidewall height (h), length (l), thickness (t), and perforation diameter (d), are systematically investigated to evaluate their effects on manufacturability and mechanical performance. The characterisations of sintered ceramic parts further elucidate the mechanism of crack formation and validate the approach in this work. Through a comprehensive consideration of fabrication limits, slurry discharge efficiency and mechanical behaviour, the honeycomb sandwich structure with optimised structural parameters exhibits superior mechanical properties after sintering, achieving more than twice the specific modulus and specific strength of the solid references with the same overall dimensions in three-point bending tests. This work provides valuable guidelines for the structural design and fabrication of honeycomb sandwich ceramic structures to achieve large-scale crack-free ceramic parts, demonstrating great promise for lightweight applications.

ARTICLE HISTORY

Received 12 September 2025
Accepted 8 November 2025

KEYWORDS

Digital light processing; 3D printing; large-scale ceramics; honeycomb structure; sintering defect

1. Introduction

Ceramic materials are extensively used in aerospace [1–4], electronics [5–7], biomedical engineering [8–10], and many other fields [11–14] due to their high strength, stiffness, and excellent thermal and chemical stability [15–17]. Additive manufacturing (AM), also known as 3D printing, offers greater flexibility in fabricating ceramic parts with complex geometries compared to conventional methods such as dry pressing [18,19], injection moulding [20,21], and tape casting [22,23]. Among various AM techniques, digital light processing (DLP) has emerged as one of the most promising technologies for fabricating intricate ceramic parts due to its high printing resolution and production efficiency. However, for large-scale ceramic parts with bulk/wall thicknesses of several tens of millimetres, the debinding process becomes particularly challenging [24,25], as the thermal decomposition of organics releases gaseous products that accumulate within the green body,

generating internal stresses that induce pores, micro-cracks, and delamination [26]. This issue tends to be more pronounced in DLP 3D-printed ceramics, where the inherently weak interlayer bonding regions are prone to microcracking under such stresses; during the subsequent sintering stage, nonuniform shrinkage and thermal gradients can further aggravate these defects, leading to macroscopic cracking and even the formation of new flaws [26]. These obstacles collectively pose a significant challenge to the reliable fabrication of large-scale ceramic parts.

To mitigate failure risks in large-scale ceramic parts during debinding and sintering, researchers have proposed several approaches: (1) incorporating non-reactive ingredients followed by low – temperature pre-debinding to create microchannels that facilitate pyrolysis product evacuation and reduce internal stresses [24,27]; (2) extending the debinding time to minimise defect formation [28,29]; (3) fully embedding the

CONTACT Rong Wang  wangr8@sustech.edu.cn  Shenzhen Key Laboratory for Additive Manufacturing of High-Performance Materials, Department of Mechanical and Energy Engineering, Southern University of Science and Technology, Shenzhen 518055, People's Republic of China; Qi Ge  geq@sustech.edu.cn  Shenzhen Key Laboratory for Additive Manufacturing of High-Performance Materials, Department of Mechanical and Energy Engineering, Southern University of Science and Technology, Shenzhen 518055, People's Republic of China

© 2025 The Author(s). Published by Informa UK Limited, trading as Taylor & Francis Group
This is an Open Access article distributed under the terms of the Creative Commons Attribution-NonCommercial License (<http://creativecommons.org/licenses/by-nc/4.0/>), which permits unrestricted non-commercial use, distribution, and reproduction in any medium, provided the original work is properly cited. The terms on which this article has been published allow the posting of the Accepted Manuscript in a repository by the author(s) or with their consent.

ceramic green bodies in ceramic powder to achieve a more moderate debinding rate and uniform temperature distribution, thereby enhancing part quality [30]. However, since these approaches primarily focus on material modification and thermal process optimisation, their adaptability in different material systems is constrained and may also reduce production efficiency. Moreover, these approaches still face the risks of failure as the part size increases, and in previous works [24,31,32], the maximum size of solid ceramic parts is limited to approximately 20 mm. In this context, structural design provides an alternative approach to mitigate the risks of cracking during the thermal treatment of large-scale ceramic parts [33].

Honeycomb sandwich structures, known for their high specific strength [34] and tunable anisotropic stiffness [35,36], have been widely applied in the lightweight design of various materials [37–39]. Furthermore, the honeycomb structure is a representative type of lattice structures [40]. The research on this structure can be easily extended to other similar structures. However, traditional design strategies for honeycomb structures have primarily focused on optimising mechanical performance or other functional properties [41–43], with little attention paid to the influence of structural parameters on cracking during debinding and sintering of ceramic parts. In ceramic DLP printing, numerous isolated chambers in honeycomb sandwich structures can trap a significant amount of uncured slurry, which is difficult to remove. Therefore, it is necessary to redesign the honeycomb sandwich structures and conduct systematic studies on slurry discharge efficiency and structural mechanical performance, to enable the manufacturing of large-scale, high-performance, and defect-free ceramic parts.

Here, we report a simple yet versatile approach that enables the fabrication of large-scale ceramic parts. The approach involves designing the interior of the parts as honeycomb structures with perforated sidewalls to mitigate defect formation during debinding and sintering processes. In this approach, the honeycomb structure effectively reduces the bulk/wall thickness of the printed body, thereby shortening the diffusion path of pyrolysis products during debinding and ultimately mitigating the issue. Perforations in the sidewalls interconnect the honeycomb chambers, facilitating the discharge of slurry within the honeycomb structure. We have designed a series of models to assess the manufacturing limits of the honeycomb sandwich structures and systematically investigated the effects of various structural parameters on slurry discharge efficiency and the mechanical properties after sintering. For the sintered ceramic parts, the evolution mechanism and

morphological characteristics of the cracks have been revealed clearly by micro-computed tomography (micro-CT) and scanning electron microscope (SEM) experiments. Three-point bending tests show that the optimised honeycomb sandwich specimens exhibit more than twice the specific strength and specific modulus of the solid references with the same overall dimensions. Finite element analysis (FEA) further elucidates the relationship between structural parameters and mechanical properties. This work demonstrates a feasible strategy for significantly increasing the achievable size of ceramics without compromising the structural integrity of the outer surfaces, providing valuable guidance for the design and fabrication of large-scale ceramic honeycomb sandwich structures with great potential for lightweight applications.

2. Materials and methods

2.1. Raw materials and slurry preparation

Al_2O_3 powder (3.98 g/cm^3 , $d_{50} = 0.5 \mu\text{m}$, Shanghai Meipai Industrial Co., Ltd., China), 1,6-hexanediol diacrylate (HDDA, Bide Pharmatech Ltd., China), and polyethylene glycol diacrylate (PEGDA, $M_w = 400$, Shanghai Macklin Biochemical Co., Ltd., China) were used as raw materials. Diphenyl(2,4,6-trimethylbenzoyl) phosphine oxide (TPO, Bide Pharmatech Ltd., China) was used as photoinitiator, and KOS110 (Guangzhou Kangoushuang Trade Co., Ltd., China) as dispersant. Initially, the required mass of Al_2O_3 powder was calculated based on the target volume fraction, ranging from 40 vol% to 55 vol% in increments of 5 vol%. HDDA, PEGDA, and Al_2O_3 powder were mixed with corresponding weight ratios. A fixed resin composition was used with HDDA: PEGDA mass ratio of 8: 2. The TPO dosage was 1 wt% relative to the resin, and the dispersant (KOS110) was 5 wt% relative to the mass of Al_2O_3 . Then the mixture was homogenised at 2000 rpm for 240 s and vacuum degassed under the absolute pressure approximately 2 kPa in a single step using a vacuum planetary mixer (ZYMC-180HV, Shenzhen Zhongyi Technology Co., Ltd., China), followed by milling in a three-roll mill (ZYTR-50T, Shenzhen Zhongyi Technology Co., Ltd., China) to obtain homogeneous photosensitive slurries with different solid loadings.

2.2. Fabrication of ceramic honeycomb sandwich structures

All Al_2O_3 samples were printed on a self-built DLP-based ceramic 3D printing apparatus with a layer thickness of 30 μm and a UV light intensity of 2.8 mW/cm² at a

wavelength of 405 nm. After printing, the residual slurry trapped in the cavities of the honeycomb structure was removed using a self-built flushing apparatus. Then, the green bodies underwent debinding at 550°C for 3 h in argon, and were subsequently sintered at 1600°C for 2.5 h in air to obtain dense ceramic parts. A tube furnace (GSL-1700X, Hefei Kejing, China) and a muffle furnace (KSL-1700X, Hefei Kejing, China) were employed to perform debinding and sintering processes, respectively.

2.3. Characterisation of ceramic slurry and green body

The viscosity of ceramic slurries was measured at 25°C using a rheometer (Discovery HR-3, TA Instruments, USA) with parallel plates (diameter of 20 mm and gap size of 200 µm) over a shear rate of 0.1-1000 s⁻¹. For photorheological experiments, a UV light source (405 nm, 8.8 mW/cm²) was attached to the rheometer to measure the photorheological properties, with the gap between the parallel plates set to 200 µm. The thermal gravimetric analysis (TGA, SDT Q600, TA Instruments, USA) was carried out in argon with a flow rate of 100 mL/min at a heating rate of 10°C/min. Morphological observations were conducted with an optical microscope (DM401, TOMLOV, USA).

2.4. Crack characterisation of sintered ceramic parts

Microstructural characterisation was performed using a field emission scanning electron microscope (Apreo2 S Lovac, Thermo Fisher Scientific, Czech Republic) operated at an accelerating voltage of 5 kV. Before observation, the samples were sputter-coated with a thin layer of platinum using a vacuum coater (Q150TES, Quorum, UK) to enhance conductivity. Micro-computed tomography (micro-CT) analysis was conducted using a high-resolution micro-CT system (SkyScan 1172, Bruker, Belgium) operated at an X-ray source voltage of 80 kV and a current of 100 µA. The exposure time was set to 5 s, and the voxel size resolution was 13 µm. The acquired 3D visualisation, as well as defect segmentation, was performed using Dragonfly software (Object Research Systems, Canada).

2.5. Mechanical test

Three-point bending experiments of the ceramic honeycomb sandwich structures were conducted using the MTS machine (Model 43, MTS Systems Corporation, USA) equipped with a 10 kN load cell under a crosshead

speed of 0.1 mm/min at room temperature. The samples were loaded along the vertical direction (printing direction). Five samples of each group were tested.

2.6. Slurry removal experiment

The efficiency of slurry removal from honeycomb sandwich structures with different perforation diameters was evaluated using a self-built flushing apparatus consisting of a rack fabricated by FDM printer (P1S, Bambu Lab, Shenzhen, China), a peristaltic pump (293KC/ZL-12V600R, JIHPUMP, Chongqing, China) provided a constant flow rate of 88 mL/min, a water tank, connecting pipes, and a microcontroller unit (Arduino Nano, Arduino, Italy) with a relay (JQC3F-05VDC-C, Weixin Electronics, Shenzhen, China) for timing control. The removal efficiency was determined by measuring the change in specimen mass during the flushing process.

2.7. Finite element analysis

To investigate the mechanical performance of the sintered specimens, we use the commercial software ABAQUS/Explicit (V6.14, Dassault Systèmes Simulia Corp., USA) to simulate the three-point bending process. Since the ceramic is a brittle material, we adopted a brittle-fracture failure criterion in the numerical simulations. This criterion is quite suitable for glass and ceramics. In this criterion, when the stress at an integration point reaches the material's fracture strength, local failure is triggered, and the corresponding finite element is deleted. This approach allows us to identify the crack initiation site during the simulation process. The material parameters of the ceramic were obtained from the three-point bending experiment.

3. Results and discussions

3.1. Defect evolution mechanism and the fabrication approach for large-scale, crack-free 3D printing ceramic parts

The 3D-printed ceramic green body is a composite of ceramic powder and polymer matrix, which could be converted to a ceramic part after debinding and sintering processes, but the thermal treatment process of 3D-printed large-scale green bodies often leads to noticeable defects in the final ceramic parts.

Figure 1(a) illustrates the crack formation and microstructural evolution mechanism of large-scale solid ceramic parts during debinding and sintering. In the green bodies, micropores may remain due to the inherently high viscosity of the ceramic slurry, which prevents

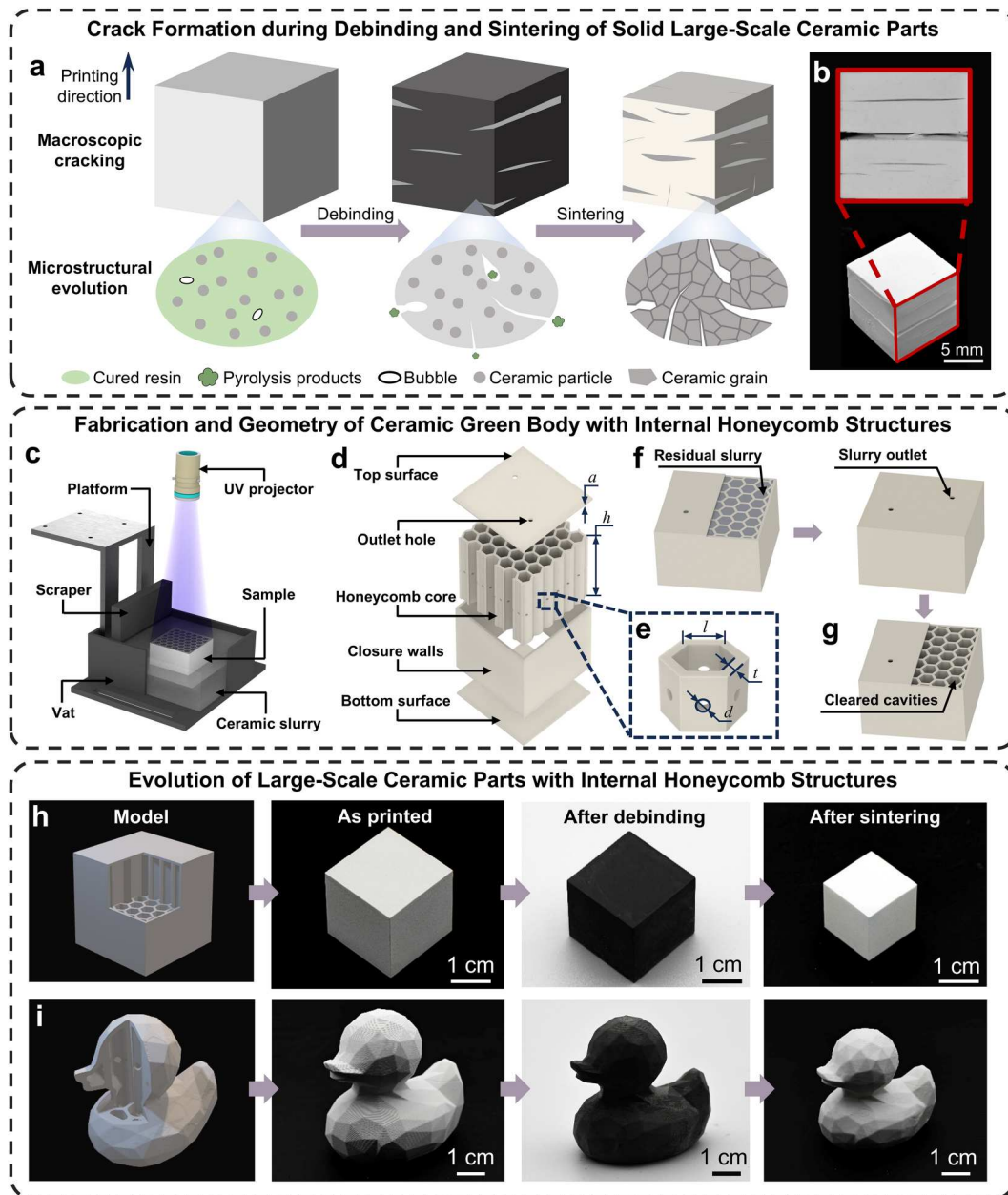


Figure 1. Defect evolution mechanism, fabrication approach for crack-free parts, and structural features of large-scale, crack-free 3D-printed ceramic parts. (a) Schematic presentation of crack evolution during debinding and sintering. (b) Photograph of typical crack morphologies in ceramic parts. (c) Illustration of the DLP-based 3D printing apparatus. (d-e) An exploded view and geometry parameters of the ceramic green body with internal honeycomb structures. (f-g) The slurry removal process and the cleared cavities. (h-i) Evolution of large-scale ceramic parts with internal honeycomb structures from modelling to printing, debinding, and sintering.

the complete removal of entrapped bubbles during printing. In the debinding stage, the polymer undergoes pyrolysis and produces gaseous products that diffuse to the surface of the green part through void channels. When the generation rate of gaseous products exceeds the diffusion rate, these gaseous products accumulate within the body, leading to an increase in internal stress and ultimately resulting in the initiation of microcracks. In DLP printing, the interlayer bonding regions of the green body exhibit relatively weak strength, making

them preferential sites for microcrack initiation and propagation. Furthermore, the pre-existing pores within the green body can also evolve into microcracks. In the sintering stage, the part undergoes significant and anisotropic volume shrinkage, during which initial cracks further propagate and evolve into macroscopic cracks. In addition, new cracks may also be generated in this process due to non-uniform shrinkage and thermal gradients. Figure 1(b) presents the typical morphology of cracks owing to thermal treatment in large-scale 3D-

printed ceramic parts, where cracks are primarily distributed along the interlayer bonding regions and extend in the direction perpendicular to the printing orientation. This indicates that these regions are preferential sites for crack initiation and growth, further confirming that the local internal stress increase caused by gas accumulation during debinding and the non-uniform shrinkage during sintering are the primary factors responsible for crack formation.

As illustrated in Figure 1(c), we print the large-scale green parts with internal honeycomb using a self-built high-resolution DLP-based 3D printer. In this system, an ultraviolet (UV) projector projects digitised UV light patterns to selectively cure the ceramic slurry containing photosensitive resin in a vat, and 3D objects are constructed in a top-down, layer-by-layer manner on the build platform. Due to the high viscosity and poor self-leveling properties of the ceramic slurry, the system is equipped with a scraper to ensure uniform coating of the slurry. Figure 1(d) shows the structure of the printed part, which is a honeycomb sandwich structure with a closure edge essentially, consisting of a top surface with slurry outlets, a honeycomb core with perforated sidewalls, peripheral closure walls and a bottom surface. The geometric parameters of the honeycomb core shown in Figure 1(d-e) include the outer wall thickness (a), core height (h), cell edge length (l), wall thickness (t), and sidewall perforation diameter (d). Figure 1(f-g) illustrates the slurry removal process, in which the residual ceramic slurry trapped in the cavities of the honeycomb structure during printing is evacuated through the perforations on the honeycomb sidewalls and outlets of the top surface. Figure 1(g) shows the cleared cavities after complete slurry removal.

Figure 1(h-i) presents the fabrication process of a cuboid with an edge length reaching 20 mm and a low-polygon ceramic duck with a maximum cross-section of 45 mm × 30 mm, detailing key stages including model design, printing, debinding, and sintering. Throughout this process, the parts maintain good structural integrity and surface quality from the green state to the final ceramic part, with no visible cracks observed, thereby verifying the reliability of this method for fabricating large-scale, crack-free ceramic parts.

3.2. Slurry characterisation and fabrication process optimisation

In general, increasing the solid loading of ceramic slurry improves the quality of the sintered parts, but also raises the slurry viscosity, thereby making printing more difficult. Figure 2(a) shows the rheological properties of ceramic slurries with solid loading from 40 vol% to 55

vol%. The viscosity increases with solid loading, and all slurries exhibit shear-thinning behaviour. Specifically, the viscosity of the 45 vol% slurry decreases from 0.81 Pa·s to 0.42 Pa·s as the shear rate increases from 10^{-1} s $^{-1}$ to 10^3 s $^{-1}$. Figure 2(b) presents the photorheological behaviour of the 45 vol% slurry. At the beginning of the experiment, the liquid slurry exhibits low storage modulus (G') and loss modulus (G''), with G'' greater than G' . Upon UV exposure, both G' and G'' increase rapidly, whereas G' rises more sharply. The intersection of G' and G'' denotes the gel point, at which the slurry transitions from a liquid to a solid state. Figure 2(c) compares the gel point transition times at different solid loadings. Under the same light intensity, the gel point transition time increases with solid loading. However, excessive exposure energy can lead to overcuring, which is detrimental to dimensional accuracy. Considering its balanced rheological and photorheological performance, along with its acceptable solid loading, the 45 vol% slurry is selected for printing.

To improve the quality of green parts, a critical consideration is the layer thickness during printing. Thinner layers generally provide higher forming accuracy and better surface quality. Common layer thickness settings are 0.10 mm or 0.05 mm. In this work, a layer thickness of 0.03 mm is used. Empirically, the curing depth is typically designed to be 2–3 times the layer thickness to obtain strong interlayer bonding and avoid excessive internal stress [44]. As illustrated in Figure 2(d), we design a ladder-type structure [45] with the bridge suspended between two side supports for the quantitative measurement of curing depth at different exposure energies. The printed part in Figure 2(e) was fabricated at a light intensity of 2.8 mW/cm 2 . The relationship between the curing depth (C_d) and exposure energy can be derived from Beer-Lambert's law [45–47]:

$$C_d = S_d \cdot \ln\left(\frac{E}{E_c}\right), \quad (1)$$

where S_d is the depth sensitivity determined by the intrinsic property of the slurry, and E_c is the critical energy density. Figure 2(f) shows the experimental result of curing depth as a function of exposure energy, which can be fitted as:

$$C_d = 53.82 \cdot \ln\left(\frac{E}{8.74}\right). \quad (2)$$

The cure depth exhibits a good linear relationship with $\ln E$. The critical energy density E_c is 8.74 mJ/cm 2 . At an exposure time of 11 s, the curing depth reaches \sim 80 μ m, corresponding to 2.7 times the layer thickness. Based on these results, a light intensity of 2.8 mW/cm 2

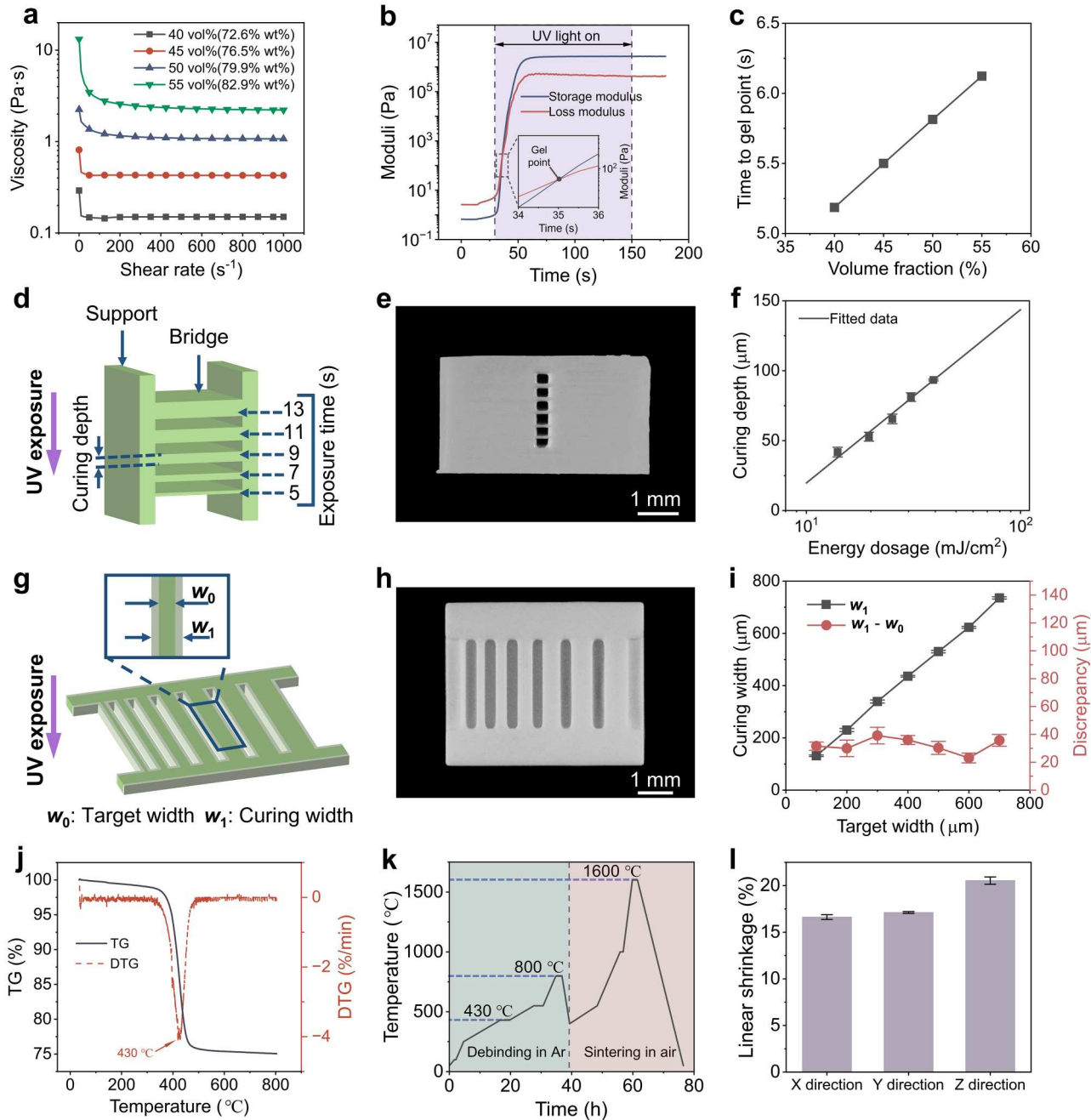


Figure 2. Characterisation and process optimisation for ceramic slurry printing and thermal treatment. (a) Rheological curves of ceramic slurries with solid loadings ranging from 40 vol% to 55 vol% (corresponding Al₂O₃ weight fractions of 72.6 wt%, 76.5 wt%, 79.9 wt%, and 82.9 wt%). (b) Photorheological curves of the 45 vol% slurry. (c) The time to gel point as a function of solid loading. (d) Schematic of vertical ladder-type structure designed to measure curing depth. (e) Printed vertical ladder-type structure. (f) The curing depth as a function of exposure energy. (g) Schematic of a horizontal ladder-type structure designed to measure printing discrepancy. (h) Printed horizontal ladder-type structure. (i) Measured line widths and corresponding deviations from the target values. (j) TG-DTG curves of the printed green body. (k) Debinding and sintering schedules conducted under different gas atmospheres. (l) Linear shrinkage ratios of the final sintered parts along the X, Y, and Z directions.

and an exposure time of 11 s are selected for subsequent printing.

Another factor limiting high-quality parts is that the honeycomb core is composed of thin-walled structures, which are highly sensitive to overcuring during printing. This results in a significant deviation of the printed

sidewall thickness from the target value. The issue is particularly pronounced in ceramic printing due to UV light scattering by ceramic particles. Therefore, in addition to optimising printing settings to control overcuring, dimensional compensation is necessary to improve geometric accuracy. To quantify the discrepancy, a

horizontal ladder-type structure with 7 lines is designed ([Figure 2\(g\)](#)) and printed ([Figure 2\(h\)](#)). The target line width (w_0) ranges from 0.10 mm to 0.70 mm, with a 0.30 mm gap between adjacent lines. However, due to the effect of overcuring, the actual line width (w_1) exceeds the target width (w_0). We define the discrepancy as excessive width ($\Delta w = w_1 - w_0$). As shown in [Figure 2\(i\)](#), measurements reveal a consistent excessive width of ~ 0.03 mm. Therefore, a pre-compensation value of 0.03 mm can be applied to improve geometric accuracy.

The printed green body contains a substantial proportion of organic constituents that must be removed through debinding, followed by high-temperature sintering (1600°C) to produce the final ceramic part. To optimise the debinding process, the thermogravimetric (TG) and differential thermogravimetric (DTG) analyses were conducted to study the thermal decomposition of organics. As shown in [Figure 2\(j\)](#), the TG-DTG curves indicate that the organic constituents decompose primarily between 300–500°C, with a maximum rate near 430°C. At 800°C, the total mass loss reaches $\sim 25\%$. The result is basically consistent with the composition of the selected slurry, which contains a ceramic mass fraction of 76.5 wt% (corresponding to a volume fraction of 45 vol%). According to the TG-DTG results, a two-step heat treatment process is conducted as shown in [Figure 2\(k\)](#). The green bodies are heated gradually to 100°C at a rate of 0.5°C/min, and held for 30 min to completely remove the residual water in cavities. Subsequently, the temperature climbs to 250°C at 1°C/min and then to 430°C at a rate of 0.25°C/min, and is held for 3 h to promote pyrolysis. Then the temperature rises to 550°C at a rate of 0.25°C/min, and is held for 3 h. Finally, the temperature increases to 800°C at 2°C/min, and is held for 2 h before cooling down to 400°C in 2.5 h. The debinded body evolves a porous network structure composed of ceramic particles and exhibits minor linear shrinkage of $\sim 3\%$. For efficiency, the debinding and sintering processes are performed sequentially in a single tube furnace under different gas atmospheres, minimising unnecessary cooling and reheating. In the sintering stage, the temperature increases to 1000°C at a rate of 0.25°C/min, and is held for 1 h. Then the temperature climbs to the peak of 1600°C in 3 h, and is maintained at this temperature for 100 min. After these steps, the ceramic parts are cooled down to room temperature in a tube furnace. The linear shrinkage of the sintered samples is presented in [Figure 2\(l\)](#). The results show anisotropic linear shrinkage behaviour: the X and Y directions exhibit similar shrinkage ratios, whereas the Z direction (printing direction) exhibits markedly higher shrinkage. The anisotropic shrinkage is mainly attributed to the layer-by-layer

printing process in the ceramic additive manufacturing, in which the weak interlayer bonding increases both the size and density of interfacial pores, resulting in more pronounced shrinkage along the printing direction [[48,49](#)].

3.3. Manufacturing limits and performance evaluation

Based on the optimised slurry composition and process parameters, we systematically investigate the fabrication limits and corresponding performance of various structural parameters, including the outer surface thickness (a), cell height (h), cell side length (l), cell sidewall thickness (t), and sidewall perforation diameter (d), under the current processing conditions. The results provide useful guidelines for structural design.

3.3.1. Effect of green body thickness on crack evolution and mechanical properties

In ceramic honeycomb structures, the outer surface thickness has a significant influence on mechanical properties. However, excessive thickness may induce defects during debinding and sintering, thereby reducing the structure's strength and stiffness. To evaluate this effect, three-point bending tests were conducted ([Figure 3\(a\)](#)). The test specimens, shown in [Figure 3\(b\)](#), had a total length (L_T) of 60 mm and a square cross section with both width and thickness equal to a ($a = 1\text{--}5$ mm). The ratio of span (L) to thickness (a) was kept constant across all samples.

[Figure 3\(c\)](#) presents the load-deflection curves for different thickness (a). Both the maximum load and deflection generally rise as a increases, although the deflection decreases when $a = 5$ mm. The flexural modulus (E) and flexural strength (σ_f) are calculated as:

$$E = \frac{L^3 F}{4a^4 \delta}, \quad (3)$$

$$\sigma_f = \frac{3F_{\max} L}{2a^3}, \quad (4)$$

where E is the flexural modulus, L is the support span, F is the load, a is the thickness of specimens, δ is the sample deflection, σ_f is the fracture strength, and F_{\max} is the fracture load.

[Figure 3\(d\)](#) shows the E and σ_f of samples with different a . When the thickness exceeds 3 mm, the flexural modulus gradually decreases from ~ 200 GPa to ~ 100 GPa. The flexural strength (σ_f) is more sensitive to thickness variations, which is about 350 MPa at $a = 1$ mm, but drops sharply to below 120 MPa when a reaches 5 mm. [Figure 3\(e\)](#) shows the corresponding

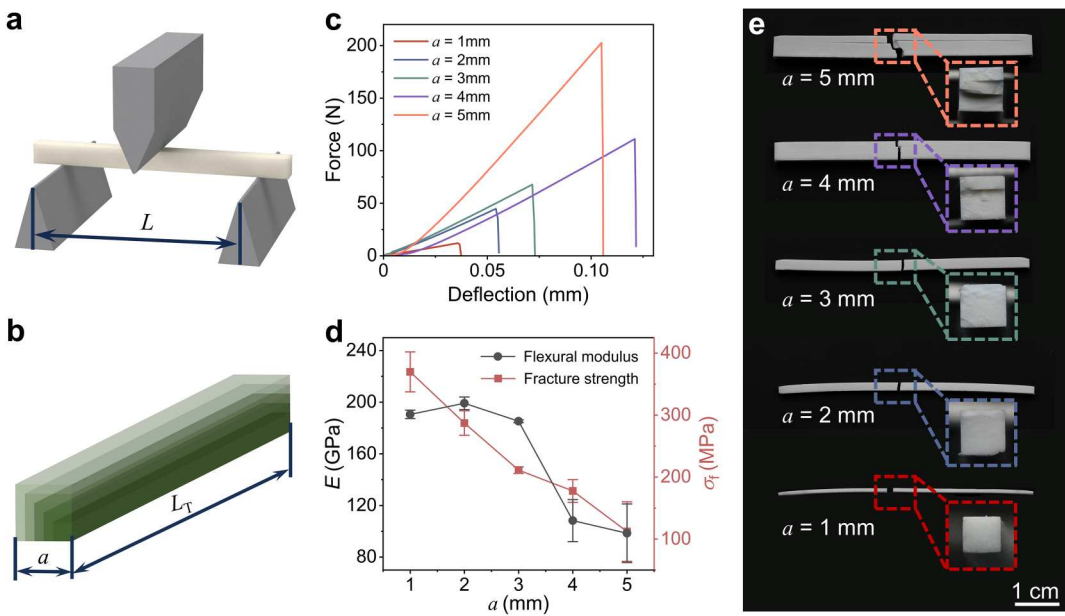


Figure 3. Mechanical properties of ceramic samples with different thicknesses. (a) Schematic of the three-point bending test. (b) Geometry of the bending test specimens. (c) Load-deflection curves of samples with different thicknesses. (d) The flexural modulus (E) and fracture strength (σ_f) of samples with different thicknesses. (e) Optical images of fractured samples and corresponding fracture morphologies.

fracture morphologies. Samples with smaller thickness exhibit good surface integrity and neat fracture surfaces. As the thickness increases, obvious defects and irregular fracture surfaces appear, resulting in reductions in both modulus and strength. These results highlight the importance of carefully controlling the outer surface thickness in ceramic honeycomb structures to achieve a balance between mechanical performance and manufacturability.

As mentioned, the thickness of the green body has a significant influence on the properties of the sintered ceramic product. This is because the intrinsic brittleness of ceramics makes them highly sensitive to cracks. With increasing green body thickness, more cracks tend to generate during the debinding and sintering processes. To investigate the relationship between the number and size of cracks in the final ceramic products and the green body thickness, the micro-computed tomography (micro-CT) and scanning electron microscope (SEM) analyses were conducted on ceramic rods with square cross-sections ranging from 1 mm to 5 mm. Figure 4(a) shows the micro-CT images in which cracks are highlighted in red. No cracks are observed in the 1 mm edge-length sample. As the edge length increases beyond 2 mm, cracks gradually become more pronounced. The increase in crack size can be clearly seen in the SEM images (Figure 4(b)), where the size increases from $\sim 20 \mu\text{m}$ to $\sim 150 \mu\text{m}$ as the edge length increases from 3 mm to 5 mm. These cracks lead to the deterioration of mechanical properties. Therefore, in the design of

the honeycomb structure, the wall thickness is set to below 1 mm to effectively avoid crack formation.

3.3.2. Fabrication limits of the core sidewalls

The honeycomb core is composed of periodic unit cells, whose sidewall thickness (t), side length (l), and height (h) are critical parameters governing the geometric feature and mechanical properties of the structure. To systematically study the manufacturability limits associated with these parameters, we design a manufacturability assessment and verification structure (MAVS), as illustrated in Figure 5(a). The MAVS adopts a ladder-type layout to emulate thin-walled honeycomb geometries with varying parameters. Within each MAVS model, all thin walls share the same thickness (t), while their height (h) increases along the negative X direction from 0.6 mm to 3.6 mm, and their length (l) increases along the negative Y direction from 0.5 mm to 3.0 mm. The Z direction corresponds to the printing direction.

Figure 5(b-c) shows optical images of MAVS parts with t of 0.1 and 0.2 mm, respectively, revealing that variations in t , h , and l gradually influence the printing quality of the thin walls. As illustrated in Figure 5(d), printing quality is classified into no deformation (ND), minor deformation (MD), and large deformation (LD). Figures 5(e-f) present two-dimensional discrete heatmaps that evaluate printing quality within the (l , h) parameter space defined for each t value. For MAVS with $t = 0.1 \text{ mm}$, deformation severity increases with both l and h . Pronounced deformation or even structural failure

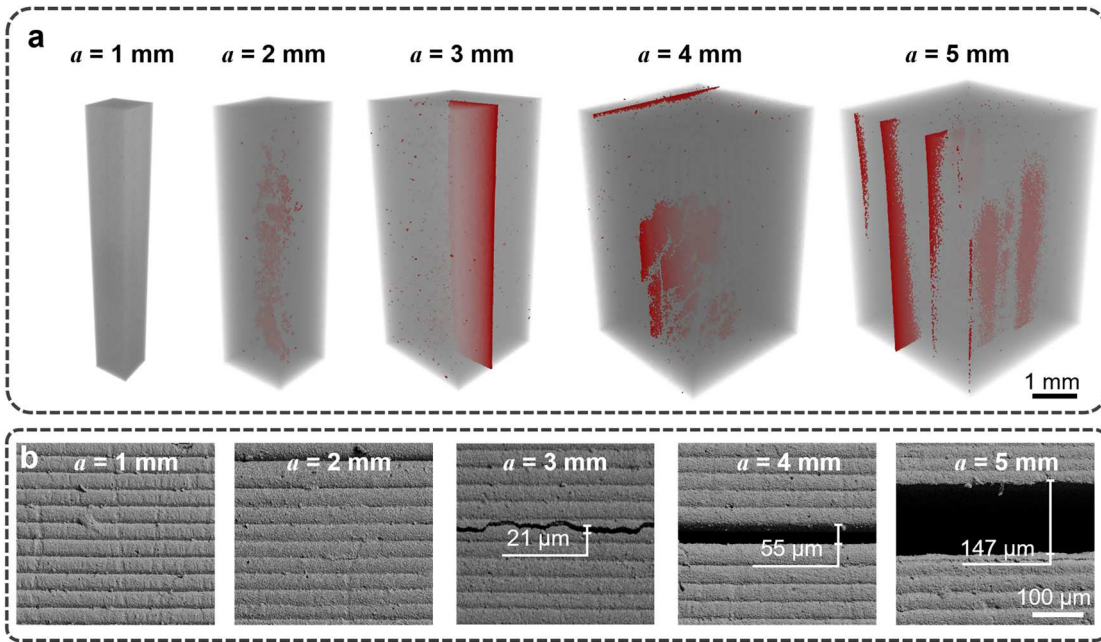


Figure 4. Micro-CT and SEM images of sintered ceramic parts with different dimensions. (a) 3D reconstructed CT images showing the internal crack distribution (highlighted in red) with different designed thicknesses. (b) Corresponding SEM surface morphologies.

may occur when $h \geq 2.4 \text{ mm}$ or $l \geq 1.5 \text{ mm}$. In contrast, for MAVS with $t = 0.2 \text{ mm}$, no notable deformation is observed within the tested parameter range. Overall, this method provides a clear framework for determining the design and fabrication boundaries of honeycomb sidewall length and height for a given wall thickness, as well as the minimum wall thickness required for specified length and height values.

3.3.3. Perforation size limit in fabrication and its influence on slurry removal efficiency

As aforementioned, perforations are introduced into the sidewalls of the ceramic honeycomb core to discharge residual slurry trapped in the internal cavities during printing. However, vertical perforations with circular features face more significant challenges in forming quality, as actual dimensions can markedly deviate from design values. This issue becomes more critical for small-sized perforations, where the circular features may disappear completely due to overcuring and distortion, resulting in blockage of the discharge pathway and thus preventing slurry removal. As illustrated in Figure 6(a), based on previous printing settings, we design a structure with d ranging from 0.12 mm to 0.93 mm in increments (Δ) of 0.09 mm, to systematically evaluate perforation quality in sidewalls. The printing direction is perpendicular to the normal direction of the circular holes. Figure 6(b) presents a series of printed specimens. The enlarged view highlights the distortion of perforations, which leads to a reduction in perforation area. Notably, the

smallest perforation ($d = 0.12 \text{ mm}$) failed to form completely.

Among all perforation characteristics, the perforation area is of primary concern, which decides the slurry removal efficiency. However, due to the distortions in perforations, measuring the area directly from the optical micrograph becomes hard. Therefore, a machine vision approach is employed, as presented in Figure 6(c). The original images are preprocessed through binarization and morphological operations; the inner contours of the perforations are then extracted to calculate the pixel areas, which are converted to actual areas using a pre-determined scale factor.

Figure 6(d) shows the relationship between the measured actual area (A_1) and target area (A_0), along with the corresponding relative discrepancies. The relative discrepancy (ϵ) is calculated as:

$$\epsilon = \frac{|A_1 - A_0|}{A_0} \times 100\%. \quad (5)$$

The relative discrepancy exhibits a strong inverse relationship with the designed area (A_0). A pronounced change occurs when the designed perforation diameter drops below 0.48 mm (corresponding to an area of 0.18 mm^2). Perforations that failed to form are marked with a 'x' symbol in the plot.

To investigate the relationship between the perforation area and the efficiency of residual slurry removal, an experimental device is designed and constructed as illustrated in Figure 7(a). This apparatus consists of a

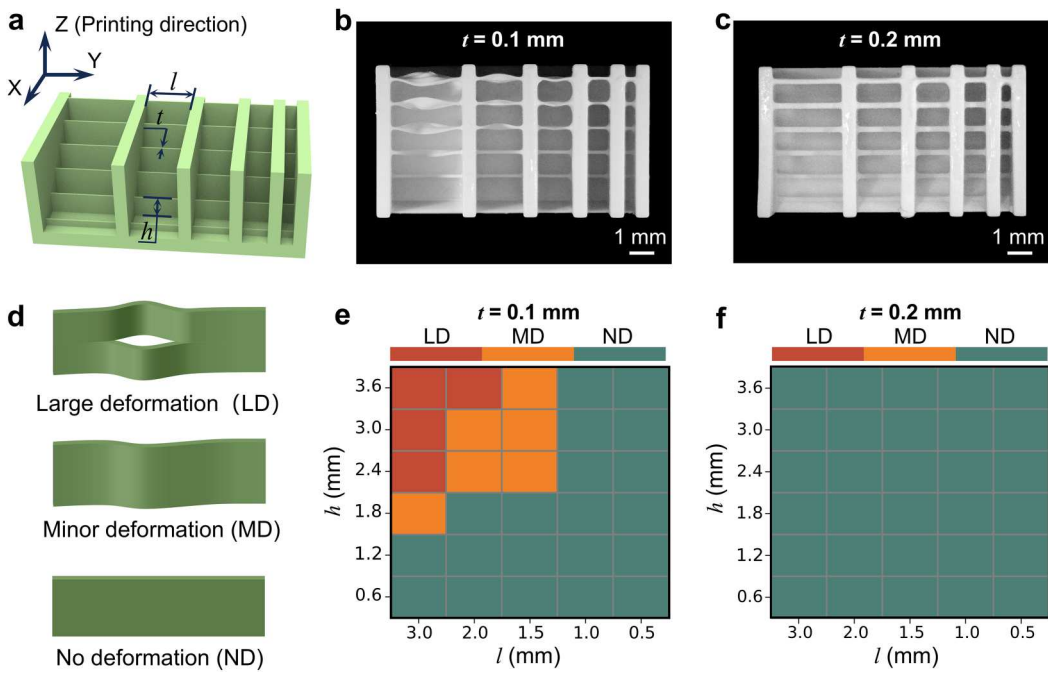


Figure 5. Manufacturability assessment and verification structure (MAVS) for determining fabrication limits of honeycomb core side-walls. (a) Schematic design of MAVS. (b-c) Optical images of printed MAVS specimens with $t = 0.1$ and 0.2 mm, respectively. (d) Classification of printing quality: no deformation (ND), minor deformation (MD), and large deformation (LD). (e-f) Two-dimensional discrete heatmaps showing printing quality within the (l , h) parameter space for different t values.

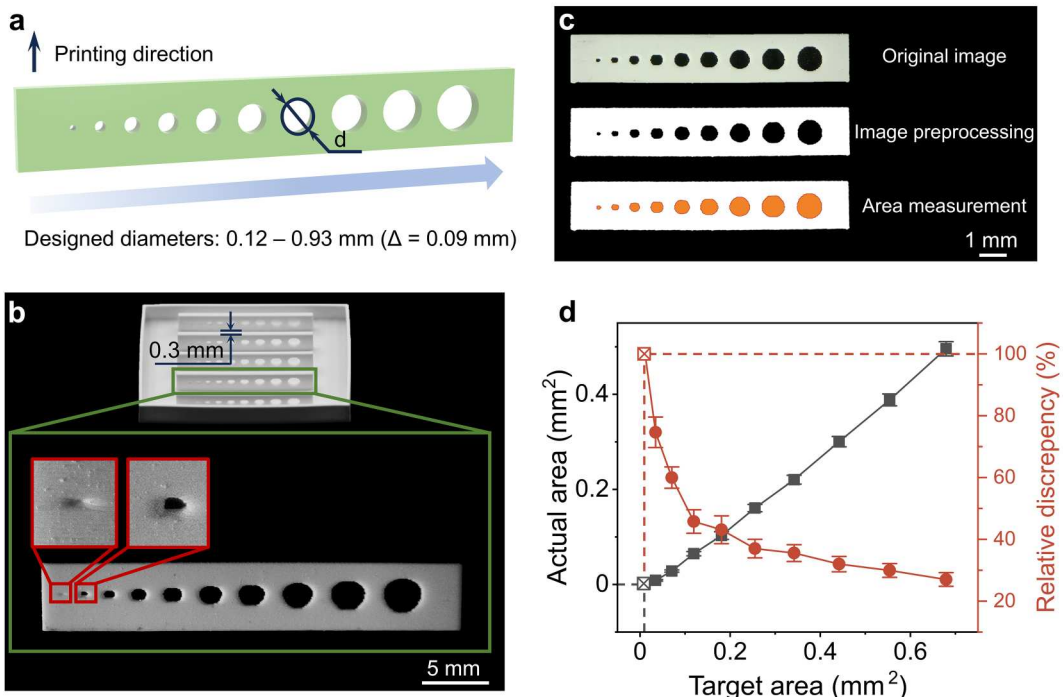


Figure 6. Printing quality evaluation of vertical perforations. (a) Schematic of the test structure for evaluating the influence of perforation diameter (d) on forming quality. (b) Printed sample with perforations of various diameters. The enlarged micrograph highlights the defects. (c) The machine-vision-based measurement of perforation area. (d) Relationship between the measured actual area (A_1) and the designed area (A_0), along with the corresponding relative discrepancies. 'x' marks represent perforation printing failure.

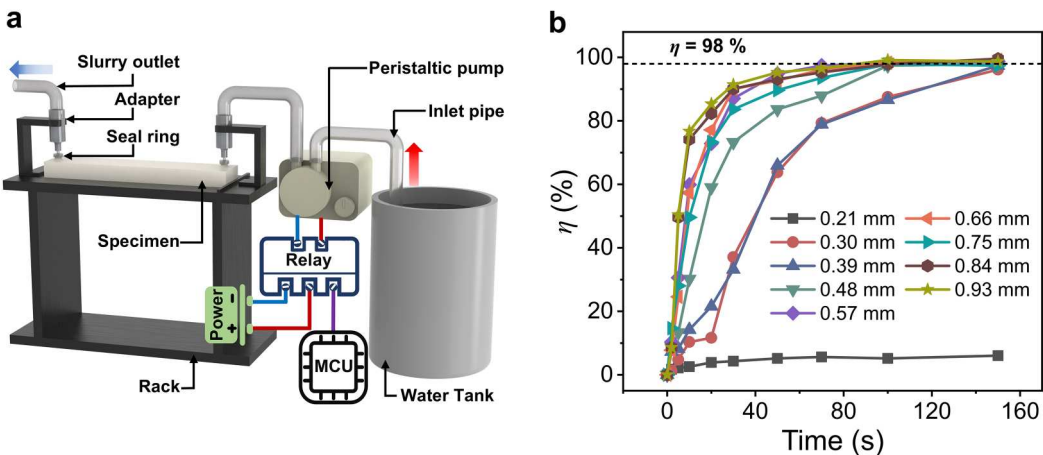


Figure 7. Experimental apparatus and flushing performance of honeycomb sandwich specimens with different perforation diameters. (a) Schematic of the flushing apparatus consisting of a rack, peristaltic pump, water tank, connecting pipes, and control system (microcontroller unit and relay). (b) The η -time curves for specimens with different perforation diameters. The dashed line indicates that the slurry removal efficiency η reaches 98%.

rack, a peristaltic pump, a water tank, pipes, and a control system. The test specimens are honeycomb sandwich structures with an overall size of 60 mm \times 12 mm \times 5 mm, in which the honeycomb cores contain perforations of various diameters. During the experiment, each specimen is placed on the rack and connected with pipes via an adapter, sealed with ethylene-vinyl acetate. The peristaltic pump delivers water from the tank into the specimen at a constant flow rate, which then exits with slurry through the outlet. The pump is powered by an external supply, and its operating time is controlled by a microcontroller unit (MCU) and relay. After flushing for a specified duration, the specimen is detached from the apparatus and weighed. The removal efficiency (η) is defined based on the change in specimen mass during the flushing process, and calculated as:

$$\eta = \frac{m_0 - m_1}{\Delta m} \times 100\%, \quad (6)$$

where m_0 is the initial mass of the specimen before flushing, m_1 is the mass at a given time during flushing, and Δm is the theoretical maximum mass change. The value of Δm is determined from the specimen's internal cavity volume. Based on the cavity volume and the slurry density (2.48 g/cm³), the theoretical mass of residual slurry inside the cavity is calculated to be ~ 3.89 g. For the same volume filled with water, the mass is 1.57 g. Since water remains inside the specimen during weighing, the maximum mass change (Δm) during flushing is 2.32 g.

Figure 7(b) presents the evolution of removal efficiency over time. The residual ceramic slurry can be considered almost completely removed when η

approaches 98%. Compared with the perforations designed with diameters of 0.30 mm and 0.39 mm, the perforation with $d = 0.48$ mm reached 98% slurry removal efficiency in a noticeably shorter time. However, for $d \geq 0.48$ mm, the time required to reach $\eta = 98\%$ is nearly independent of perforation diameter. This threshold corresponds to the sharp change in relative area discrepancy indicated in Figure 6(d). In particular, although the perforation with $d = 0.21$ mm can be printed, it exhibits negligible slurry removal efficiency in practice.

Overall, the perforation diameter in the sidewalls of the honeycomb sandwich structure is closely associated with slurry removal efficiency. Undersized perforations not only suffer severe dimensional deviation due to overcuring and forming defects, but also cause a significant drop in removal efficiency. In the settings mentioned above, the minimum printable perforation diameter is approximately 0.21 mm. However, to ensure both geometric accuracy and effective slurry removal, the designed perforation diameter should be no less than 0.30 mm, and a diameter of 0.48 mm is recommended for ideal slurry removal efficiency.

3.3.4. Three-point bending performance of large-scale solid and honeycomb ceramic specimens

To systematically evaluate the mechanical performance of the designed ceramic honeycomb sandwich structures, several ceramic specimens were fabricated, and three-point bending tests were conducted. As illustrated in Figure 8(a), the span length is fixed at $L = 40$ mm. The experimental specimens are divided into three groups: a solid reference and two types of ceramic honeycomb sandwich structures (CHSS) featuring representative

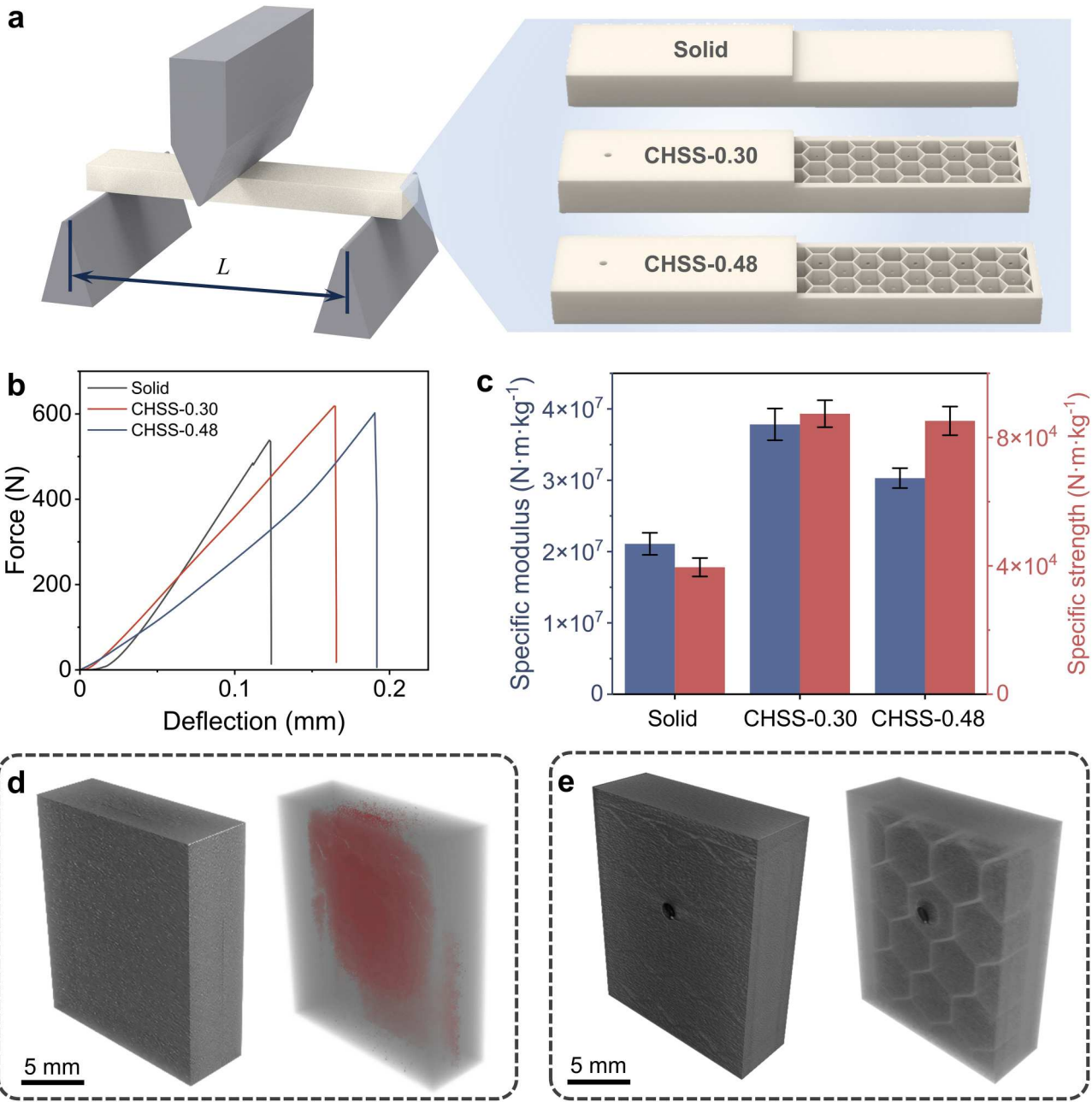


Figure 8. Three-point bending tests and micro-CT characterisation of solid and honeycomb ceramic specimens. (a) Schematic of the three-point bending test and representative sintered ceramic specimens: solid reference, CHSS-0.30 (perforation diameter $d = 0.30$ mm), and CHSS-0.48 ($d = 0.48$ mm). (b) Force-deflection curves of the tested specimens. (c) Specific modulus and specific strength of different specimens. (d) Micro-CT images of solid specimen with internal cracks (highlighted in red). (e) Micro-CT images of honeycomb sandwich structure without visible internal cracks.

perforation diameters. One type has a diameter of 0.30 mm (CHSS-0.30), which represents the smallest size of perforation to discharge the residual slurry; the other has a diameter of 0.48 mm (CHSS-0.48), at which the slurry evacuation efficiency reaches a plateau and is therefore regarded as the critical dimension for structural design. The overall size of the sintered specimens is about 50 mm \times 10 mm \times 4 mm, with a structural apparent density is $\sim 2.31\text{ g}/\text{cm}^3$ and corresponding to a

solid volume fraction of $\sim 59.5\%$ (porosity of 40.5%) relative to the fully solid structure.

Figure 8(b) shows the typical force-deflection curves for different specimens. The solid specimen exhibits the lowest load-bearing capacity and deflection compared with the ceramic honeycomb sandwich structures of equal external dimensions, which can be attributed to the cracks generated during the debinding and sintering. Figure 8(c) presents the specific modulus and

specific strength, which are ratios of flexural modulus and flexural strength to apparent density of the corresponding specimen. Compared with the solid specimens, both the CHSS-0.30 and CHSS-0.48 exhibit markedly stronger specific modulus and specific strength. Notably, CHSS-0.30 represents slightly superior mechanical performance to CHSS-0.48, indicating that smaller perforation sizes are preferable for enhancing mechanical properties. The micro-CT images in Figure 8(d-e) show that the solid specimen contains numerous cracks, while no cracks are observed in the honeycomb sandwich structure. Thus, the honeycomb structural design is effective in mitigating or preventing crack formation during the debinding and sintering processes,

thereby facilitating improvements in mechanical properties.

To further investigate the relationship between the perforation sizes and mechanical performance, a numerical simulation is conducted. In the simulation process, to remain consistent with the physical experimental conditions, the numerical model was constructed from the green-body geometry (the overall design size is $60 \text{ mm} \times 12 \text{ mm} \times 5 \text{ mm}$, outer wall thickness $a = 1 \text{ mm}$, sidewall thickness of honeycomb unit cell $t = 0.20 \text{ mm}$, and cell side length $l = 2 \text{ mm}$). The dimensions of the model were adjusted in each principal direction according to the anisotropic shrinkage ratios to obtain geometry sizes that were close to those of the

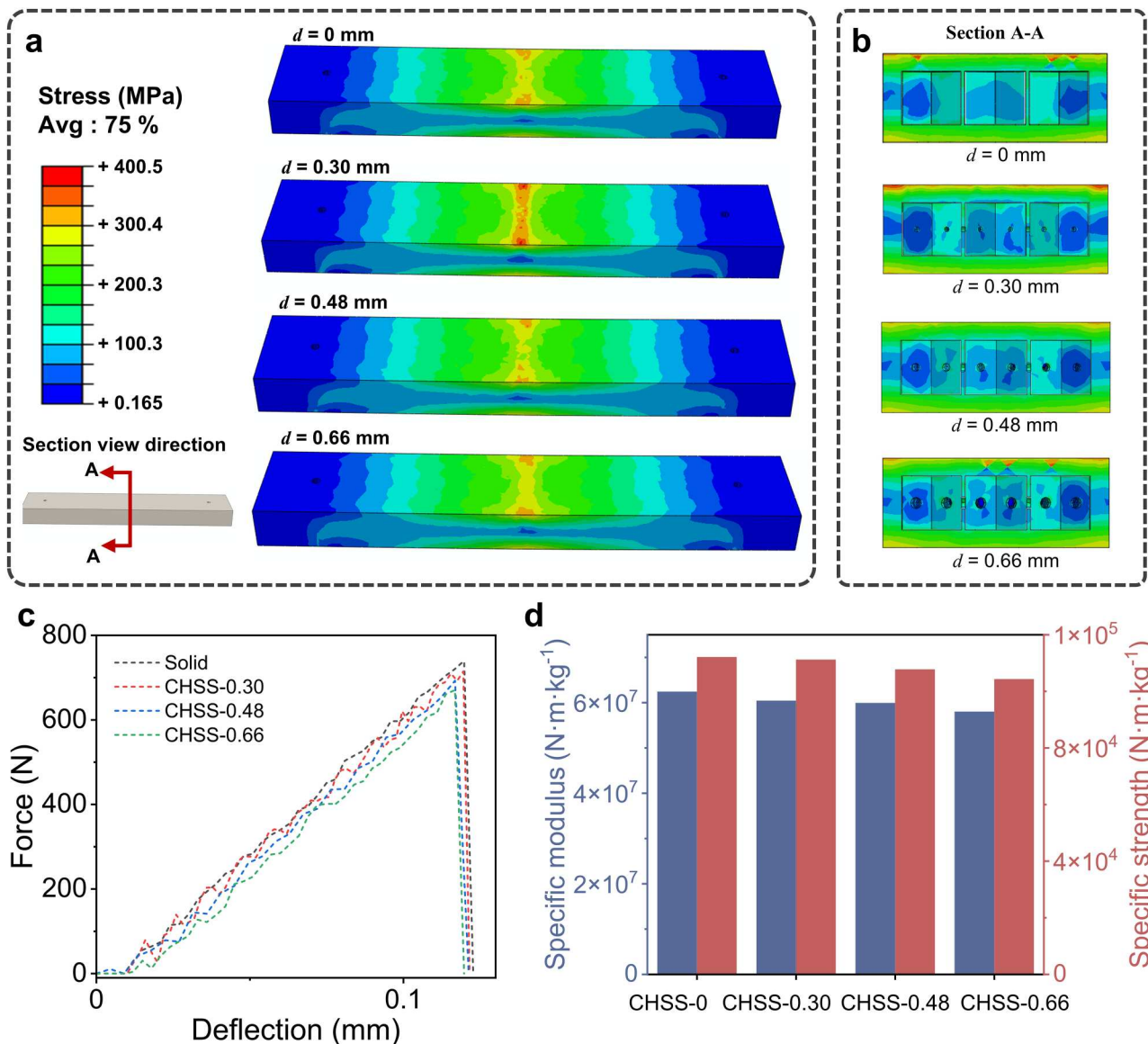


Figure 9. Simulation of the perforated honeycomb specimens under three-point bending. (a) Stress contour maps showing the von Mises stress distribution of specimens with $d = 0, 0.30, 0.48, 0.66 \text{ mm}$. (b) Stress distribution at corresponding loading states on the section A-A. (c) Load-deflection curves of simulations with different perforation diameters. (d) Comparison of specific modulus and specific strength for simulations with different perforation diameters.

sintered specimens (overall size: $50 \text{ mm} \times 10 \text{ mm} \times 4 \text{ mm}$). The side-wall perforation diameter was set to $d = 0 \text{ mm}$ (no perforation), 0.30 mm , 0.48 mm , and 0.66 mm . Loading and boundary conditions matched the three-point bending experiments (identical span, loading rate, and other related experimental conditions).

Figure 9(a) shows the stress distribution map on the specimens at the moment before failure. The corresponding structural cross-section at this moment is shown in **Figure 9(b)**, where the stress concentration is around the perforation edges, yet the local stress there is much lower than the tensile stress at the outer surfaces. Therefore, the crack initiation occurs at the outer surfaces rather than at the edge of the perforation. **Figure 9(c-d)** presents the force-deflection curves obtained from the three-point bending simulations and the corresponding specific modulus and specific strength of specimens with different perforation diameters. The plots indicate that the mechanical performance decreases slightly with increasing perforation diameter, but the overall reduction is not substantial and aligns well with the experimental results.

4. Conclusions

In this work, we introduce a honeycomb core with side-wall perforation into DLP-printed ceramic parts to mitigate defect formation during debinding and sintering, thereby facilitating the fabrication of large-scale ceramics. The critical point of this approach is that it transforms the ceramic material distribution of large ceramic parts from a continuous to a discontinuous form with an internal honeycomb structure, thereby artificially shortening the path of releasing the pyrolysis product during the debinding process and enabling the fabrication of crack-free, large-scale ceramic parts. There are two advantages of this approach: (1) it allows for the lightweight fabrication of large-scale ceramics; (2) it preserves an intact outer surface to enhance its overall applicability.

Through experimental validation, we determine the appropriate slurry solid loading and optimal printing parameters, providing a foundation for investigating the fabrication limits of the structure and evaluating its mechanical performance. The results reveal that outer wall thickness (a) significantly affects flexural strength, which decreases from $\sim 350 \text{ MPa}$ to below 120 MPa as the thickness increases from 1 mm to 5 mm . Additionally, the manufacturability of honeycomb sidewalls is influenced by sidewall thickness (t), height (h), and length (l), with thicker sidewalls resulting in better fabrication quality. Perforation diameter (d) is also a key parameter, as smaller diameters cause more severe dimensional deviations and hinder effective slurry removal.

For the sintered ceramic parts, micro-CT and SEM images reveal the mechanism of crack formation and evolution. The effectiveness of the honeycomb design in mitigating or avoiding crack formation is proved through the comparison between the solid and honeycomb sandwich structures in micro-CT scanning and mechanical properties. Three-point bending tests demonstrate that ceramic honeycomb sandwich structures with $a = 1 \text{ mm}$, $h = 3.6 \text{ mm}$, $l = 2.0 \text{ mm}$, $t = 0.20 \text{ mm}$, and $d = 0.30 \text{ mm}$ exhibit more than twice the specific modulus and specific strength of solid references with the same overall dimensions, highlighting their potential for lightweight applications. Furthermore, to elucidate the relationship between the key parameter perforation diameter and mechanical performance, a numerical simulation is conducted. The simulation results show that the perforation size has a minor effect on the three-point bending performance. Overall, this work presents a strategy that maintains a relatively intact outer surface while substantially enlarging the manufacturable size of crack-free ceramic parts. It further proposes a systematic approach to evaluating the fabrication limits of key geometric parameters in the honeycomb structures, offering guidance for enhancing the manufacturing quality and mechanical performance of ceramic parts.

Acknowledgements

Qi Ge acknowledges the National Key Research and Development Program of China (Grand No. 2023YFB4605400) and the National Natural Science Foundation of China (Grand No. 12472152). Rong Wang acknowledges the National Natural Science Foundation of China (Grand No. 52575396).

Author contributions

CRedit: **Siqian Wu:** Conceptualization, Data curation, Formal analysis, Investigation, Visualization, Writing – original draft; **Rong Wang:** Conceptualization, Formal analysis, Funding acquisition, Visualization, Writing – review & editing; **Liuchao Jin:** Data curation, Methodology; **Xingjian Huang:** Investigation, Resources; **Wuzhao Li:** Investigation, Visualization; **Kun Zhou:** Formal analysis, Resources, Writing – review & editing; **Qi Ge:** Formal analysis, Funding acquisition, Project administration, Supervision, Writing – review & editing.

Disclosure statement

No potential conflict of interest was reported by the author(s).

Funding

This work was financially supported by the National Key Research and Development Program of China (grant number:

2023YFB4605400), and the National Natural Science Foundation of China (grant number: 52575396 & 12472152).

ORCID

Siqian Wu  <http://orcid.org/0009-0009-5682-1346>
 Rong Wang  <http://orcid.org/0000-0002-2780-0206>
 Kun Zhou  <http://orcid.org/0000-0001-7660-2911>

Data availability statement

The data that support the findings of this study are openly available in Figshare at: <https://doi.org/10.6084/m9.figshare.30437198>.

References

- [1] Liu G, Zhao Y, Wu G, et al. Origami and 4D printing of elastomer-derived ceramic structures. *Sci Adv.* **2018**;4(8): eaat0641. doi:[10.1126/sciadv.aat0641](https://doi.org/10.1126/sciadv.aat0641)
- [2] Huang W, Xue Z, Li L, et al. In-situ formed intergranular TiB₂ into lightweight SiC (rGO) composite PDCs enable elevated temperature resistance for aerospace components. *J Alloys Compd.* **2023**;937:168377. doi:[10.1016/j.jallcom.2022.168377](https://doi.org/10.1016/j.jallcom.2022.168377)
- [3] Padture NP. Advanced structural ceramics in aerospace propulsion. *Nat Mater.* **2016**;15(8):804–809. doi:[10.1038/nmat4687](https://doi.org/10.1038/nmat4687)
- [4] Feng X, Guo F, Luo L, et al. Engineering design of feedstock powder and relevant thermal-mechanical performance of thermal/environmental barrier coatings. *J Adv Ceram.* **2025**;14(2). doi:[10.26599/JAC.2025.9221033](https://doi.org/10.26599/JAC.2025.9221033)
- [5] Liu W, Zheng T, Zhou Z, et al. Ultrahigh piezoelectricity and temperature stability in piezoceramics by synergistic design. *Nat Commun.* **2025**;16(1):1527. doi:[10.1038/s41467-025-56798-7](https://doi.org/10.1038/s41467-025-56798-7)
- [6] Gao X, Cheng Z, Chen Z, et al. The mechanism for the enhanced piezoelectricity in multi-elements doped (K, Na) NbO₃ ceramics. *Nat Commun.* **2021**;12(1):881. doi:[10.1038/s41467-021-21202-7](https://doi.org/10.1038/s41467-021-21202-7)
- [7] Li F, Lin D, Chen Z, et al. Ultrahigh piezoelectricity in ferroelectric ceramics by design. *Nat Mater.* **2018**;17(4):349–354. doi:[10.1038/s41563-018-0034-4](https://doi.org/10.1038/s41563-018-0034-4)
- [8] Xu F, Ren H, Zheng M, et al. Development of biodegradable bioactive glass ceramics by DLP printed containing EPCs/BMSCs for bone tissue engineering of rabbit mandible defects. *J Mech Behav Biomed Mater.* **2020**;103:103532. doi:[10.1016/j.jmbbm.2019.103532](https://doi.org/10.1016/j.jmbbm.2019.103532)
- [9] Zhao M, Yang D, Fan S, et al. 3D-Printed strong dental crown with multi-scale ordered architecture, high-precision, and bioactivity. *Adv Sci.* **2022**;9(5):2104001. doi:[10.1002/advs.202104001](https://doi.org/10.1002/advs.202104001)
- [10] Shan Y, Bai Y, Yang S, et al. 3D-printed strontium-incorporated β-TCP bioceramic triply periodic minimal surface scaffolds with simultaneous high porosity, enhanced strength, and excellent bioactivity. *J Adv Ceram.* **2023**;12(9):1671–1684. doi:[10.26599/JAC.2023.9220787](https://doi.org/10.26599/JAC.2023.9220787)
- [11] Wang R, Yuan C, Cheng J, et al. Direct 4D printing of ceramics driven by hydrogel dehydration. *Nat Commun.* **2024**;15(1):758. doi:[10.1038/s41467-024-45039-y](https://doi.org/10.1038/s41467-024-45039-y)
- [12] Li J, Shen Z, Chen X, et al. Grain-orientation-engineered multilayer ceramic capacitors for energy storage applications. *Nat Mater.* **2020**;19(9):999–1005. doi:[10.1038/s41563-020-0704-x](https://doi.org/10.1038/s41563-020-0704-x)
- [13] Chen S, Wang R, Li H, et al. High-precision BaTiO₃ piezoelectric ceramics via vat photopolymerization 3D printing. *J Eur Ceram Soc.* **2024**;44(14):116706. doi:[10.1016/j.jeurceramsoc.2024.116706](https://doi.org/10.1016/j.jeurceramsoc.2024.116706)
- [14] Wang R, Ye H, Cheng J, et al. Ultrastrong and damage-tolerant ceramic architectures via 3D printing. *Addit Manuf.* **2023**;61:103361. doi:[10.1016/j.addma.2022.103361](https://doi.org/10.1016/j.addma.2022.103361)
- [15] Zhu J, Ren Q, Chen C, et al. Vacancies tailoring lattice anharmonicity of Zintl-type thermoelectrics. *Nat Commun.* **2024**;15(1):2618. doi:[10.1038/s41467-024-46895-4](https://doi.org/10.1038/s41467-024-46895-4)
- [16] Zheng S, Wu W, Zhang Y, et al. Enhancing surface activity and durability in triple conducting electrode for protonic ceramic electrochemical cells. *Nat. Commun.* **2025**;16(1):4146. doi:[10.1038/s41467-025-59477-9](https://doi.org/10.1038/s41467-025-59477-9)
- [17] Sciti D, Vinci A, Zoli L, et al. Elevated temperature performance: arc-jet testing of carbon fiber reinforced ZrB₂ bars up to 2200°C for strength retention assessment. *J Adv Ceram.* **2025**;14(2):9221022. doi:[10.26599/JAC.2024.9221022](https://doi.org/10.26599/JAC.2024.9221022)
- [18] Qin Z, Xu X, Xu T, et al. High-strength thermal insulating porous mullite fiber-based ceramics. *J Eur Ceram Soc.* **2022**;42(15):7209–7218. doi:[10.1016/j.jeurceramsoc.2022.08.050](https://doi.org/10.1016/j.jeurceramsoc.2022.08.050)
- [19] Liu C-L, Du Q, Zhang C, et al. Fabrication and properties of BaTiO₃ ceramics via digital light processing for piezoelectric energy harvesters. *Addit Manuf.* **2022**;56:102940. doi:[10.1016/j.addma.2022.102940](https://doi.org/10.1016/j.addma.2022.102940)
- [20] Didilis K, Marani D, Bihlet UD, et al. Freeform injection molding of functional ceramics by hybrid additive manufacturing. *Addit Manuf.* **2022**;60:103197. doi:[10.1016/j.addma.2022.103197](https://doi.org/10.1016/j.addma.2022.103197)
- [21] Wick-Joliat R, Tschamper M, Kontic R, et al. Water-soluble sacrificial 3D printed molds for fast prototyping in ceramic injection molding. *Addit Manuf.* **2021**;48:102408. doi:[10.1016/j.addma.2021.102408](https://doi.org/10.1016/j.addma.2021.102408)
- [22] Du W, Lu K, He B, et al. Direct tape casting of Al₂O₃/AlN slurry for AION transparent ceramic wafers via one-step reaction sintering. *J Eur Ceram Soc.* **2023**;43(8):3538–3543. doi:[10.1016/j.jeurceramsoc.2023.01.056](https://doi.org/10.1016/j.jeurceramsoc.2023.01.056)
- [23] Jiang Z, Wang S, Chen X, et al. Tape-casting Li_{0.34}La_{0.56}TiO₃ ceramic electrolyte films permit high energy density of lithium-metal batteries. *Adv Mater.* **2020**;32(6):1906221. doi:[10.1002/adma.201906221](https://doi.org/10.1002/adma.201906221)
- [24] Wu Y, Chen X, Zhao G, et al. Development of thick-walled ceramic parts via vat photopolymerization using low-viscosity non-reactive diluent as an additive. *Addit Manuf.* **2025**;97:104607. doi:[10.1016/j.addma.2024.104607](https://doi.org/10.1016/j.addma.2024.104607)
- [25] Santoliquido O, Camerota F, Ortona A. The influence of topology on DLP 3D printing, debinding and sintering of ceramic periodic architectures designed to replace bulky components. *Open Ceram.* **2021**;5:100059. doi:[10.1016/j.oceram.2021.100059](https://doi.org/10.1016/j.oceram.2021.100059)
- [26] Wu X, Teng J, Ji X, et al. Research progress of the defects and innovations of ceramic vat photopolymerization. *Addit Manuf.* **2023**;65:103441. doi:[10.1016/j.addma.2023.103441](https://doi.org/10.1016/j.addma.2023.103441)

- [27] Kim J, Gal CW, Choi Y-J, et al. Effect of non-reactive diluent on defect-free debinding process of 3D printed ceramics. *Addit Manuf.* **2023**;67:103475. doi:[10.1016/j.addma.2023.103475](https://doi.org/10.1016/j.addma.2023.103475)
- [28] Scheithauer U, Schwarzer E, Moritz T, et al. Additive manufacturing of ceramic heat exchanger: opportunities and limits of the lithography-based ceramic manufacturing (LCM). *J Mater Eng Perform.* **2018**;27:14–20. doi:[10.1007/s11665-017-2843-z](https://doi.org/10.1007/s11665-017-2843-z)
- [29] Sun J, Binner J, Bai J. 3D printing of zirconia via digital light processing: optimization of slurry and debinding process. *J Eur Ceram Soc.* **2020**;40(15):5837–5844. doi:[10.1016/j.jeurceramsoc.2020.05.079](https://doi.org/10.1016/j.jeurceramsoc.2020.05.079)
- [30] Li H, Liu Y, Liu Y, et al. Effect of burying sintering on the properties of ceramic cores via 3D printing. *J Manuf Process.* **2020**;57:380–388. doi:[10.1016/j.jmapro.2020.07.007](https://doi.org/10.1016/j.jmapro.2020.07.007)
- [31] Pfaffinger M, Mitteramskogler G, Gmeiner R, et al. Thermal debinding of ceramic-filled photopolymers. *Mater Sci Forum.* **2015**;825:75–81. doi:[10.4028/www.scientific.net/MSF.825-826.75](https://doi.org/10.4028/www.scientific.net/MSF.825-826.75)
- [32] Mohammed MK, Alahmari A, Alkhalefah H, et al. Evaluation of zirconia ceramics fabricated through DLP 3d printing process for dental applications. *Heliyon.* **2024**;10(17):e36725. doi:[10.1016/j.heliyon.2024.e36725](https://doi.org/10.1016/j.heliyon.2024.e36725)
- [33] Zuo Z, De Corte W, Huang Y, et al. Strategies towards large-scale 3D printing without size constraints. *Virtual Phys Prototyp.* **2024**;19(1):e2346821. doi:[10.1080/17452759.2024.2346821](https://doi.org/10.1080/17452759.2024.2346821)
- [34] Zhang J, Lu G, You Z. Large deformation and energy absorption of additively manufactured auxetic materials and structures: a review. *Compos B Eng.* **2020**;201:108340. doi:[10.1016/j.compositesb.2020.108340](https://doi.org/10.1016/j.compositesb.2020.108340)
- [35] Oftadeh R, Haghpanah B, Papadopoulos J, et al. Mechanics of anisotropic hierarchical honeycombs. *Int J Mech Sci.* **2014**;81:126–136. doi:[10.1016/j.ijmecsci.2014.02.011](https://doi.org/10.1016/j.ijmecsci.2014.02.011)
- [36] Li X, Lu Z, Yang Z, et al. Anisotropic in-plane mechanical behavior of square honeycombs under off-axis loading. *Mater Des.* **2018**;158:88–97. doi:[10.1016/j.matdes.2018.08.007](https://doi.org/10.1016/j.matdes.2018.08.007)
- [37] Guo H, Yuan H, Zhang J, et al. Review of sandwich structures under impact loadings: experimental, numerical and theoretical analysis. *Thin-Walled Struct.* **2024**;196:111541. doi:[10.1016/j.tws.2023.111541](https://doi.org/10.1016/j.tws.2023.111541)
- [38] Cui Y, Zhou Q, Xu Z, et al. Structure failure and strength evaluation of honeycomb-based sandwich composites under variable hydro-thermal-mechanical load. *Compos Struct.* **2025**;354:118763. doi:[10.1016/j.compstruct.2024.118763](https://doi.org/10.1016/j.compstruct.2024.118763)
- [39] Zhang D, Fei Q, Zhang P. In-plane dynamic crushing behavior and energy absorption of honeycombs with a novel type of multi-cells. *Thin-Walled Struct.* **2017**;117:199–210. doi:[10.1016/j.tws.2017.03.028](https://doi.org/10.1016/j.tws.2017.03.028)
- [40] Khan N, Riccio A. A systematic review of design for additive manufacturing of aerospace lattice structures: current trends and future directions. *Prog Aerosp Sci.* **2024**;149:101021. doi:[10.1016/j.paerosci.2024.101021](https://doi.org/10.1016/j.paerosci.2024.101021)
- [41] Qi C, Jiang F, Yang S. Advanced honeycomb designs for improving mechanical properties: a review. *Compos Part B-Eng.* **2021**;227:109393. doi:[10.1016/j.compositesb.2021.109393](https://doi.org/10.1016/j.compositesb.2021.109393)
- [42] Yıldız BK, Yıldız AS, Kul M, et al. Mechanical properties of 3D-printed Al_2O_3 honeycomb sandwich structures prepared using the SLA method with different core geometries. *Ceram Int.* **2024**;50(2):2901–2908. doi:[10.1016/j.ceramint.2023.11.028](https://doi.org/10.1016/j.ceramint.2023.11.028)
- [43] Kafkaslioğlu Yıldız B. Assessment of mechanical performance of Al_2O_3 ceramic honeycomb sandwich structures produced with SLA 3D-printing regarding unpolymerized slurry removal strategy. *J Aust Ceram Soc.* **2024**;60(4):1199–1208. doi:[10.1007/s41779-024-01021-x](https://doi.org/10.1007/s41779-024-01021-x)
- [44] Johansson E, Lidström O, Johansson J, et al. Influence of resin composition on the defect formation in alumina manufactured by stereolithography. *Materials.* **2017**;10(2):138. doi:[10.3390/ma10020138](https://doi.org/10.3390/ma10020138)
- [45] He X, Wang R, Qi S, et al. Vat photopolymerization 3D printing of polymer-derived SiOC ceramics with high precision and high strength. *Addit Manuf.* **2023**;78:103889. doi:[10.1016/j.addma.2023.103889](https://doi.org/10.1016/j.addma.2023.103889)
- [46] Griffith ML, Halloran JW. Freeform fabrication of ceramics via stereolithography. *J Am Ceram Soc.* **1996**;79(10):2601–2608. doi:[10.1111/j.1151-2916.1996.tb09022.x](https://doi.org/10.1111/j.1151-2916.1996.tb09022.x)
- [47] Wang R, Cui Y, Ye H, et al. Vat photopolymerization 3D printing of alumina ceramics with low sintering temperature. *Ceram Int.* **2024**;50(21):42434–42443. doi:[10.1016/j.ceramint.2024.08.089](https://doi.org/10.1016/j.ceramint.2024.08.089)
- [48] You S, Jiang D, Wang F, et al. Anisotropic sintering shrinkage behavior of stainless steel fabricated by extrusion-based metal additive manufacturing. *J Manuf Processes.* **2023**;101:1508–1520. doi:[10.1016/j.jmapro.2023.07.026](https://doi.org/10.1016/j.jmapro.2023.07.026)
- [49] Manière C, Kerbart G, Harnois C, et al. Modeling sintering anisotropy in ceramic stereolithography of silica. *Acta Mater.* **2020**;182:163–171. doi:[10.1016/j.actamat.2019.10.032](https://doi.org/10.1016/j.actamat.2019.10.032)